
Feature Identification via the Empirical NTK

Jennifer Lin

PIBBSS

jylin04@gmail.com

Abstract

We provide evidence that eigenanalysis of the empirical neural tangent kernel (eNTK) can surface the features used by trained neural networks. Across two standard toy models for mechanistic interpretability, Toy Models of Superposition (TMS) and a 1-layer MLP trained on modular addition, we find that the eNTK exhibits sharp spectral cliffs whose top eigenspaces align with ground-truth features. In TMS, the eNTK recovers the ground-truth features in both the sparse (high superposition) and dense regimes. In modular arithmetic, the eNTK can be used to recover Fourier feature families. Moreover, we provide evidence that a layerwise eNTK localizes features to specific layers and that the evolution of the eNTK eigenspectrum can be used to diagnose the grokking phase transition. These results suggest that eNTK analysis may provide a practical handle for feature discovery and for detecting phase changes in small models.

1 Introduction

Mechanistic interpretability seeks to understand how neural networks process information at inference time (Olah et al. [2020]). A major open question is to understand how neural networks represent learned features. Operationally, suppose that an input to a model can either exhibit a particular human-interpretable property (e.g. the color red, a dog snout) or not. Neural networks often seem to learn to detect such properties. For example, they can be probed to classify the presence or absence of such properties after pretraining with higher-than-chance accuracy (Alain and Bengio [2016]). We would like to understand how they do so internally, by finding functions of a model’s activations and weights that detect the presence of the property with high sensitivity and specificity.

It’s a priori unclear how to “guess” a good candidate answer. One strategy is to look to theories of deep learning. If there existed a hypothetical complete theory that allowed us to “reverse-compile” any model into human-interpretable code, it would (by definition) solve this problem by telling us which effective features a model uses and how they interact to produce the input-output map (Olah [2022]). Instead of a complete theory however, at present we have several nascent theories that each explain some modest aspects of what neural networks may be doing, in some corners of the parameter space.¹

Among such theories in 2025, the neural tangent kernel (NTK) and its cousins (Jacot et al. [2018], Roberts et al. [2022]) are unique in giving us a closed-form formula for the function f learned by a

¹See e.g. the examples on page 13 of Sharkey et al. [2025].

neural network in a corner of the parameter space: namely

$$f_i(x) = \sum_{\alpha_1, \alpha_2 \in \mathcal{D}} K_{ij}(x, x_{\alpha_1}) K_{jk}^{-1}(x_{\alpha_1}, x_{\alpha_2}) y_{k, \alpha_2}, \quad (1)$$

where the index i runs over output neurons (classes), α runs over points in the training set \mathcal{D} , and the data-space kernel

$$K_{ij}(x_1, x_2) = \sum_{\mu} \frac{df_i(x_1)}{dW_{\mu}} \frac{df_j(x_2)}{dW_{\mu}} \Big|_{t=t_0} \quad (2)$$

evaluated at initialization, with the index μ running over model parameters, is the eponymous NTK. Eq. (1) is a provably good approximation to the function learned by a neural network under gradient descent with MSE loss in a “lazy limit” where the drift in model parameters throughout training is parametrically small. See Appendix A for a review.

Realistic models are usually not in this regime. However, it’s been conjectured and empirically verified in some situations (Fort et al. [2020], Atanasov et al. [2021], Ortiz-Jiménez et al. [2021], Mohamadi et al. [2023]) - although we don’t yet have a general understanding of when the conjecture is and isn’t true - that Eq. (1) with the NTK (2) evaluated at the end of training instead of at initialization,

$$K_{ij}(x_1, x_2) = \sum_{\mu} \frac{df_i(x_1)}{dW_{\mu}} \frac{df_j(x_2)}{dW_{\mu}} \Big|_{t=t_*}, \quad (3)$$

can at times be a good approximation to the function learned by a neural network beyond the lazy limit. This conjecture goes by the name of the empirical NTK hypothesis (eNTK hypothesis), with (3) being the empirical NTK (eNTK).

In this paper, we will take this conjecture seriously and see if the eNTK can be used to generate new algorithms for mechanistic interpretability. In particular, we examine the hypothesis that eigenvectors of the eNTK may align with interesting features at the end of training. We find that this idea turns out to be true in toy models commonly studied by the mechanistic interpretability community. Our main contributions are that

- In “Toy Models of Superposition” (Elhage et al. [2022]), the eNTK eigenspectrum is anisotropic with a qualitatively large drop at the n th ordered eigenvalue, for n the number of ground-truth features. The leading n -dimensional eigenspace aligns nearly 1:1 with the ground-truth features at the end of training in both the sparse and dense regimes.
- For a 1L MLP trained on modular arithmetic mod p in the grokking regime, the eNTK eigenspectrum develops two cliffs. The first cliff, which is localized to the first layer of the model and visible already at initialization, has dimension $k = 4\lfloor p/2 \rfloor$ and a span that matches the Fourier features learned by the first layer of the model. A Laplacian (axis-smoothness) rotation inside this subspace yields basis vectors that exactly align with the Fourier features used by the model.
- The second cliff aligns with “sum” and “difference” Fourier features and appears precisely at the grokking phase transition. In this sense, eNTK spectral analysis provides a practical diagnostic that localizes where features live by layer and detects phase transitions.

This paper is organized as follows. In Section 2, we explain how we use the eNTK to find features in trained models. In Sections 3 and 4, we use the eNTK to find features in Toy Models of Superposition and a 1L MLP trained on modular arithmetic, respectively. We conclude with a discussion of future directions in Section 5.

Related work. A few earlier works have explored whether NTK eigenvectors align with interesting directions in trained models. Loo et al. [2022] and Tsilivis and Kempe [2022] visualized kernel eigenvectors as candidate features in small image nets (in the context of using the NTK to study adversarial training), and are the most closely related works. Atanasov et al. [2021] and Baratin et al. [2021] argued that NTK tangent features rotate towards directions predictive of the outputs during training.

Besides the eNTK, other objects involving gradients/curvature have appeared in the mechanistic interpretability literature. As mentioned above, the eNTK (3) is constructed by contracting a pair of Jacobians $J(z) = \nabla_W f(z)$ along the parameter direction, forming a kernel in data space (shorthand: $K(z, z') = J(z)J(z')^T = \nabla_W f(z)\nabla_W f(z')^T$). The Hessian, the second derivative of the loss function wrt parameters $H = \nabla_W^2 \mathcal{L}$, can be approximated by a pair of Jacobians contracted the other way ($H \approx \sum_i J(x_i)^T \nabla_f^2 \mathcal{L}(f(x_i), y_i) J(x_i)$), and appears frequently in recent work on singular learning theory (e.g Bushnaq et al. [2024]). The Hessian induces a “influence function” kernel on data points $\mathcal{I}(z', z) = -\nabla_W \mathcal{L}(z')^T H^{-1} \nabla_W \mathcal{L}(z)$ (Koh and Liang [2017]) that was recently used to interpret LLMs at scale (Grosse et al. [2023]). Somewhat further afield, attribution patching (Nanda [2023]) approximates activation patching (an interpretability technique where one swaps clean activations into a corrupted forward pass to test causal effect) by estimating the effect using the activation’s local gradient.”

The idea of approximating a neural network by keeping only kernel modes up to an emergent spectral scale can be viewed as a naive application of renormalization ideas to mechanistic interpretability (Greenspan [2025]), with the spectral scale setting a hard UV cutoff.

2 Method: NTK pipeline for feature-finding

The main idea that we pursue in this paper is to treat the eNTK as fundamental and interpret its top eigenvectors. One motivation for doing so is that empirically, the spectrum of the eNTK is often very anisotropic. (We’ll see many examples of this below.) When true, it means that *if* the linearized formula (1) is a good approximation to the function learned by a neural network at the end of training, the same formula where we replace the kernel with its low-rank spectral truncation should in turn be a good approximation, and the top eigenvectors of the kernel should contain most of the information about how the trained model computes its outputs.

Below, for several models, we will eigendecompose the empirical NTK and its variants defined in section 2.1. We define a **cliff** to be a (qualitatively) large drop in the ordered eigenvalues and a **NTK feature subspace** to be the span of eigenvectors corresponding to the eigenvalues in a cliff.

To compute if a length- N eNTK eigenvector for N the dataset size aligns with a ground-truth feature, we can take the absolute value of its cosine similarity with a length- N “feature vector” whose entries consist of that feature’s activation on each data point. This gives a scalar for each (eigenvector, feature) pair. To visualize how the eigenvectors across a NTK feature subspace align with a selection of features, we will render heatmaps that show this correlation across all pairs.

2.1 Variants of the eNTK used in this paper

The eNTK evaluated over all points in a dataset has shape (N, N, C, C) for N the size of the dataset, and C the number of output neurons (classes). To do an eigendecomposition, we must reduce it to two dimensions. Below we’ll use two collapses of K :

1. Per-class eNTK. For a class $c \in 1, \dots, C$, we can study the kernel $K_{cc}(x_1, x_2)$.

2. Flattened eNTK. Alternatively, we can form a NC by NC matrix by stacking the per-class blocks $\{K_{ij}\}_{i,j=1}^C$ row-major in i and column-major in j .

Another variant that we'll use is the layerwise NTK where rather than sum over all model parameters in (3), we sum only over those parameters belonging to a particular layer, before applying either collapse above. This will prove useful for attributing features to a layer.

3 Results for “Toy Models of Superposition”

In our first experiment, we study the alignment of eNTK eigenvectors with ground-truth features in Toy Models of Superposition (TMS) (Elhage et al. [2022]).

3.1 Review of the setup

In TMS, we train a 1L autoencoder with a smaller hidden layer size m than input/output layer size n and tied weights to learn the identity map on a dataset of n synthetic features. Explicitly, the model architecture is

$$f(x) = \text{ReLU}(W^T W x + b); \quad (4)$$

the dataset consists of N length- n vectors whose i th entry is set to 0 with probability S , and otherwise randomly drawn from $U[0, 1]$ ²; and the loss function is MSE loss modified by a per-feature importance hyperparameter I_i ,

$$\mathcal{L} = \sum_i I_i (x_i - f_i(x))^2. \quad (5)$$

The claim to fame of this setup is that it's a maximally simple toy model of superposition: i.e., the idea that *if* models store features as linear combinations of within-layer neurons, then a model might learn to represent more features than neurons available to it by storing them non-orthogonally in the neural activations. In this experiment, the n input/output directions are the analogs of ground-truth features, and one would like to see if the autoencoder is able to reconstruct them. Upon training this class of model, one finds that when the features are dense (small S), the model learns to reconstruct the top m features only, but as one dials up the sparsity, the model is able to recover more and more features, at the cost of encoding them non-orthogonally.

Our motivation is somewhat different. Namely, given a TMS model at any (m, n) (i.e. in either the sparse or dense regime), we would like to see if the eNTK eigenvectors at the end of training line up with the ground-truth features. Below we report results for models trained to convergence on a 500-point training set and hyperparameters $n = 50$ and $I_i = 0.8^i$ (with varying m and S). However, other choices of hyperparameters lead to qualitatively similar behaviors.

3.2 Results

Spectral structure and cliffs. Across TMS settings (dense vs. sparse regime and different widths m), the flattened eNTK exhibits a pronounced spectral cliff structure separating a small set of leading modes from a long tail (Fig. 1, row 1). In all cases that we tested, the leading eigenspace contains two cliffs with the second drop appearing at $k = 50$, equal to the number of ground-truth features in the dataset. A first cliff differentiates the number of features that the model is able to reconstruct from those it cannot.³

²By using a fixed-size dataset, we're actually using the setup of Henighan et al. [2023].

³Quantitatively, in each example the number of entries along the diagonal of $W^T W$ exceeding the heuristic threshold of 0.75, for W the trained weight matrix, equals the size of one of the two cliffs.

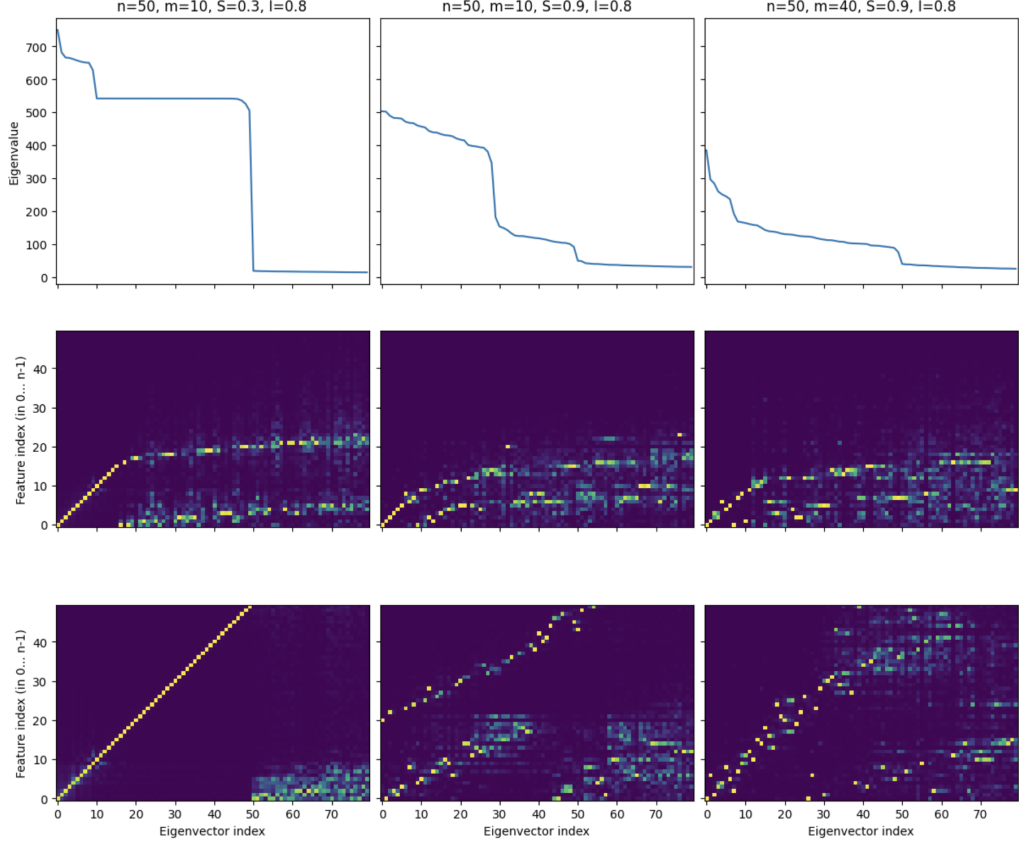


Figure 1: Eigenvalue spectrum of the flattened eNTK (top row) and column-normalized, importance-rescaled flattened eNTK eigenvector-feature indicator heatmaps for TMS models with $n = 50$ ground-truth features, importance $I_i = 0.8^i$, (hidden-layer size, sparsity) $m = 10, S = 0.3$ (left column); $m = 10, S = 0.9$ (middle column) or $m = 40, S = 0.9$ (right column); and importance rescaling parameters $\beta = 1$ (middle row) and $\beta = 0.3$ (bottom row). The center column is an example of a TMS model in the sparse regime (high superposition), while the left and right columns are two different ways to push the model to the dense regime (low superposition).

Alignment with ground-truth features. As discussed in section 2, one way to visualize how well a length- N eigenvector for N the dataset size lines up with a ground-truth feature is to compute its inner product with a “feature vector” whose entries consist of that feature’s activation on each data point. Here, we choose instead to work with the flattened eNTK which is a shape NC by NC tensor. At the same time, the output classes C correspond to ground-truth features in TMS. To construct heatmaps displaying how well the flattened eNTK eigenvectors align with ground-truth features in TMS, we therefore first build an expanded data matrix of shape (NC, C) whose entries are zero unless the class indices match, then compute and display the inner product of the expanded data matrix with the top flattened eNTK eigenvectors.

Another modification that we do ahead of rendering the heatmaps is to apply an importance rescaling to the eNTK, multiplying each Jacobian entry $df_i(x)/dW_\mu$ in (3) by $I^{\beta i/2}$. This directionally corrects for the fact that the derivation of Eq. (1) assumed a standard MSE loss (see Appendix A), but TMS uses an importance-weighted MSE loss, (5). The choice $\beta = 1$ is the theoretically principled one that absorbs I into the NTK in eq. (11), allowing the rest of the derivation in Appendix A to proceed with standard MSE, while $\beta = 0$ corresponds to turning off the importance rescaling.

With $\beta = 1$, we find that the leading eigenvectors align with *high-importance* features (middle row of Fig. 1).

We also sweep over other values of $\beta \in [0, 1]$ and find that as β decreases, lower-importance features become increasingly visible in the heatmaps. In particular, at the value $\beta = 0.3$ (bottom row of Fig. 1), the leading eigendirections of the importance-rescaled eNTK appear to align nearly one-to-one with *all* of the ground-truth features of TMS in both the sparse and dense regimes. This experiment suggests that the raw kernel also contains information about less-important features, but down-weights them in line with the objective.

In the sparse (high superposition) regime, the map between top eNTK eigenvectors and ground-truth features appears to split into two lines sorted by importance (center and bottom middle plots in Fig. 1). It could be interesting to try to understand why this happens. This is likely possible given the simplicity of the kernel itself in TMS (see Appendix B for the closed-form expression of the kernel), but we will leave it for future work.

4 Results for modular arithmetic (grokking)

Next, we study the alignment of top eNTK eigenvectors with the ground-truth Fourier features in a MLP trained on modular arithmetic (Gromov [2023]).

4.1 Review of the setup

In this experiment, for a fixed integer p we construct a dataset consisting of the (length $2p$) p^2 unique pairs of concatenated, one-hot encoded integers from $(0, \dots, p-1)$, labeled by their (length p) one-hot-encoded sum mod p . We split the dataset into non-overlapping train and test sets controlled by a fractional hyperparameter $\alpha = |\mathcal{D}_{\text{train}}|/p^2$. We then train a 1L MLP with $2p$ input neurons, n hidden neurons, p output neurons, a quadratic activation function, and no biases to learn the training set with a MSE loss function and AdamW optimizer. Explicitly, the model architecture is

$$f(x) = W^{(2)}(W^{(1)}x)^2. \quad (6)$$

In the experiments below, we report results for $p = 29$, $n = 512$ and $\alpha = 0.7$. However, we find qualitatively similar results for different values of the hyperparameters (including e.g. the narrower model with $n = 64$, 3 other values of p , and 5 different seeds).

With these hyperparameters, the model exhibits grokking (Power et al. [2022], Nanda et al. [2023]). Namely, some time after reaching 100% accuracy on the training set, it suddenly goes from 0% to 100% accuracy on the test set (see the left panel of Fig. 3), suggesting that it switched to using a more generalizable representation of the underlying modular arithmetic algorithm.

Moreover, in this case we know the exact solution that the model learns after grokking (Gromov [2023]). At the end of training, the model solves modular addition by learning the weights

$$W_{k(a,b)}^{(1)} = \begin{pmatrix} \cos(2\pi \frac{k}{p}a + \varphi_k^{(1)}) \\ \cos(2\pi \frac{k}{p}b + \varphi_k^{(2)}) \end{pmatrix}^T, \quad (7)$$

$$W_{qk}^{(2)} = \cos(-2\pi \frac{k}{p}q - \varphi_k^{(3)}), \quad (8)$$

where we represent $W_{k(a,b)}^{(1)}$ as a row of two $n \times p$ matrices, with total shape $(n, 2p)$; $k \in 0, \dots, n-1$ runs over the hidden-layer neurons and $a, b, q \in 0, \dots, p-1$ over the two input and output integers, respectively; and the phases $\varphi_k^{(i)}$ are random but should satisfy the constraints $\varphi_k^{(1)} + \varphi_k^{(2)} = \varphi_k^{(3)}$.

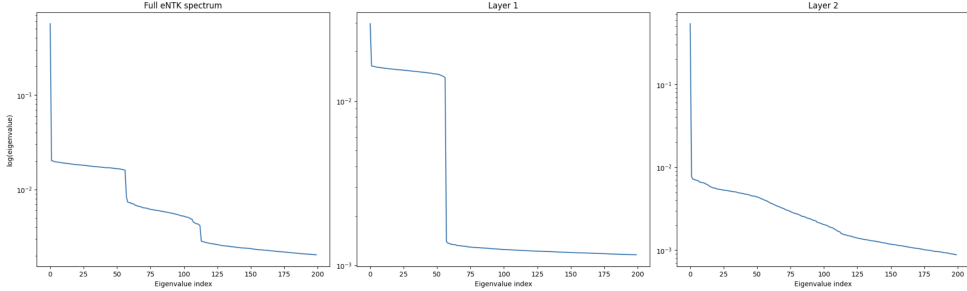


Figure 2: Full and layerwise eNTK spectrum of the modular arithmetic model after training to convergence (500 epochs). The left column displays the spectrum of the full eNTK, the middle column the spectrum of the layerwise eNTK wrt the parameters (7) in layer 1, and the right column the spectrum of the layerwise eNTK wrt the parameters (8) in layer 2.

The weights (7), (8) fully determine the neural activations at each level. In particular, given input integers a and b the first-layer preactivations are simply

$$h_k^{(1)}(a, b) = \cos\left(2\pi\frac{k}{p}a + \varphi_k^{(1)}\right) + \cos\left(2\pi\frac{k}{p}b + \varphi_k^{(2)}\right), \quad (9)$$

and the first-layer activations are its squares (see (6)). Hence, linear combinations of neural activations form Fourier features $\cos(2\pi\frac{k}{p}a)$, $\cos(2\pi\frac{k}{p}b)$ up to phase (below: the ‘‘cos a ’’ and ‘‘cos b ’’ feature families), for $k \in 1, \dots, \lfloor \frac{p}{2} \rfloor$.⁴

After applying trigonometric identities, the second-layer activations turn out to be the sum of many terms each with the schematic form $\sum_{k=1}^n \cos(2\pi\frac{k}{p}s + \varphi_k)$, for s a linear combination of $\{a, b, q\}$ and φ_k a linear combination of $\{\varphi_k^{(1)}, \varphi_k^{(2)}, \varphi_k^{(3)}\}$. For generic phases these sums cancel, but one such term turns out to use exactly the combination $\varphi_k^{(1)} + \varphi_k^{(2)} - \varphi_k^{(3)} = 0$. Hence, its phase drops out and the remaining $\sum_{k=1}^n \cos(2\pi\frac{k}{p}s)$ acts as a modular δ function, firing exactly when $s = a + b - q$.

4.2 Results

The eNTK spectrum of the modular-arithmetic model trained to convergence is shown in the left panel of Fig. 2. It contains two cliffs, each of size $56 = 4\lfloor \frac{p}{2} \rfloor$ for our choice of $p = 29$.

Layerwise localization. Using the layerwise NTK (where we restrict the sum in (3) to parameters in a single layer), we find that the first cliff localizes to layer 1 (middle panel of Fig. 2), while the second is most cleanly visible if we keep parameters from both layers 1 and 2.

Time evolution of the spectrum. The second cliff is absent before grokking and appears at the grokking phase transition (see the right panel of Fig. 3). This suggests that feature-finding aside, perhaps the eNTK can be used to find phase transitions. The eigenvectors evolve smoothly on either side of the phase transition even as the eigenvalues jump. We comment on the evolution of the eigenvectors in Appendix D.

On the other hand, the first cliff is present already at initialization (see the right panel of Fig. 3). This suggests (in combination with the subsection below) that this model’s use of Fourier modes could perhaps have been predicted at initialization from the eNTK.

⁴Fourier modes with $k > \lfloor \frac{p}{2} \rfloor$ are redundant because of trigonometric identities relating arguments x with $2\pi - x$.

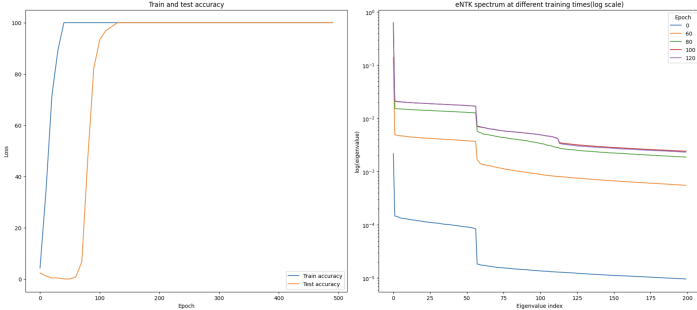


Figure 3: Spectral change at the grokking phase transition. Left: Train and test accuracy shows evidence for a grokking phase transition (sudden onset of generalization) around epoch 90. Right: at the same training time, the eNTK spectrum develops a kink at the base of the second cliff.

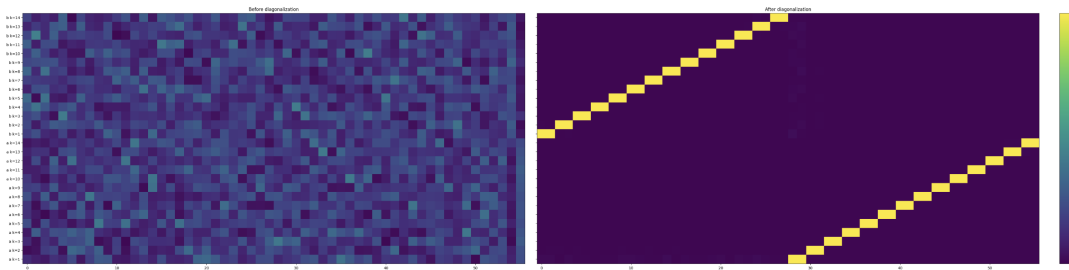


Figure 4: Results from applying the two-stage per-axis graph smoothness algorithm described in Appendix C to rotate the eNTK eigenvector basis in the Layer 1 cliff. Left: heatmap showing the squared norm of the inner product of eNTK eigenvectors in the cliff with the $(\cos a, \sin a)$ or $(\cos b, \sin b)$ feature families. Right: heatmap showing the squared norm of the inner product of basis vectors in the Layer 1 cliff found from applying the two-stage graph smoothness algorithm described in Appendix C with the $(\cos a, \sin a)$ or $(\cos b, \sin b)$ feature families.

Disentanglement. Since the cliffs have dimension $4\lfloor \frac{p}{2} \rfloor$, it seems a priori plausible that they contain Fourier feature families. (More precisely, each cosine Fourier family has size $\lfloor \frac{p}{2} \rfloor$ and comes paired with a sine family for a count of $\{\cos, \sin\} \times \{k = 1, \dots, \lfloor \frac{p}{2} \rfloor\} = 2 \lfloor \frac{p}{2} \rfloor$, so $4\lfloor \frac{p}{2} \rfloor$ has the right counting to contain two such families.) However, the heat map of inner products of the eNTK eigenvectors in the Layer 1 cliff with feature vectors for the a and b Fourier families is not 1:1. See the left-hand plot in Fig. 4, where in each square we plot the squared norm of the inner product of the i th eNTK eigenvector in the Layer 1 cliff with the $(\cos a, \sin a)$ or $(\cos b, \sin b)$ feature families.

⁵

We would like to understand if a rotation inside the first cliff eigenspace could surface the Fourier modes. Since the space of possible inputs forms a $p \times p$ toroidal lattice, we can test for this by ordering directions in the first cliff eigenspace by the magnitude of sum-of-squared differences between the images of adjacent lattice points. If the Layer 1 cliff was in fact a rotation of the Fourier modes, this way of picking a basis should separate low-frequency Fourier modes from high-frequency ones.

In practice, we apply the two-stage “per-axis graph smoothness” algorithm described in Appendix C. Upon doing so, we find cleanly that the Layer 1 cliff does in fact contain directions aligned with the a and b Fourier families. This is shown on the right-hand side of Fig. 4.

⁵This equals the maximal correlation with a phase-shifted cosine in (9), i.e. the best match over possible phases $\varphi_k^{(1)}, \varphi_k^{(2)}$.

A similar procedure shows that the second cliff appearing in the eNTK spectrum after grokking contains the $a \pm b$ Fourier families. We discuss this in Appendix D.

5 Discussion

To summarize, we have provided evidence that eigenanalysis of the eNTK can surface learned features across toy benchmarks commonly used by the mechanistic interpretability community.

There are several potentially interesting directions for follow-up work.

At the most basic level, it could be interesting to apply the pipeline presented here to other MLPs that model different aspects of realistic data. For example, we could apply our method to extensions of TMS that model composed or hierarchical features, or to toy models of feature splitting, addressing a known weakness of SAEs.

Ultimately, we would like to make contact with realistic datasets/models. For this, it will be important to extend our pipeline to Transformers. As a natural first exercise we plan to apply the pipeline to a Transformer trained on modular arithmetic, but we would also like to study how our method interacts with Transformers trained on algorithms that require nontrivial attention (e.g. induction heads (Olsson et al. [2022])), and on larger models (e.g. Bricken et al. [2023], OthelloGPT (Li et al. [2023]) and others). The latter may require advances in the underlying implementation to let us approximate the eNTK at scale.

For the 1L models studied in this paper, it's easy to write down closed-form expressions for the kernels in terms of the weights and data vectors. (See Appendix B.) It could be interesting to understand analytically what properties of said weights and data were needed to get the clean mechanistic signals presented here.

Finally, our route to recovering the Fourier features in Section 4 required imposing a geometric prior of smoothness on the input space by hand.⁶ It would be nice to be able to identify features without using any structural prior beyond the raw data. To this end, perhaps we could learn such a prior from the kernel itself in a way that could generalize to other situations.⁷

We hope to say more about these directions in the future.

Acknowledgements

I am grateful to Ari Brill, Lauren Greenspan, Andrew Mack, Logan Smith, and Dmitry Vaintrob for discussions and to Lauren Greenspan for comments on the manuscript. This work was supported by PIBSS and the Long-Term Future Fund.

A Review of NTK theory

In this section, we review the derivation of Eq. (1) since it motivates this entire line of study. As mentioned in the introduction, a main claim of the NTK theory is that a neural network trained under gradient flow with MSE loss learns the function (1), (2) at the end of training provided that its

⁶Though not full a priori knowledge of the Fourier features.

⁷For example, as a naive first idea, perhaps we could replace the algorithm in Appendix C with one that constructs a graph designating inputs to the model as “neighbors” iff their eNTK rows look similar, then runs a Laplacian rotation on the learned graph to sort the eNTK eigenvectors. However, it's not clear whether and when this idea would generalize in an interesting way to other situations.

trajectory stays in a “lazy limit” where the drift in parameters throughout training is parametrically small.

The idea behind the derivation is that if we take a limit where the changes in a model’s weights W_μ over training are small enough that we can truncate a Taylor expansion of the model in its weights to first order while maintaining a good approximation, then perhaps we can resum the **linearized approximation** to how the model changes at each step of gradient descent to get a closed-form formula for the function learned by the model.

In equations, given a neural network $f_i(x, W_\mu)$ with index i running over the output neurons, the Taylor expansion for the change in the model after a step of gradient descent is

$$f_i(x, W_\mu(t+1)) - f_i(x, W_\mu(t)) = \sum_\mu \frac{df_i(x)}{dW_\mu} \bigg|_{W_\mu=W_\mu(t)} dW_\mu + \dots \quad (10)$$

where the \dots ’s denote terms quadratic and higher in dW_μ . Using the definition of gradient descent to replace $dW_\mu \rightarrow -\eta \frac{d\mathcal{L}}{dW_\mu}$ for η the learning rate and \mathcal{L} the loss function, as well as the fact that the loss function itself depends on the model evaluated on points in the training set, we can massage (10) into

$$f_i(x, W_\mu(t+1)) - f_i(x, W_\mu(t)) = -\eta \sum_j \sum_{\alpha \in \mathcal{D}} \frac{d\mathcal{L}}{df_j(x_\alpha)} \left[\sum_\mu \frac{df_i(x)}{dW_\mu} \frac{df_j(x_\alpha)}{dW_\mu} \right] \bigg|_{W_\mu=W_\mu(t)} + \dots, \quad (11)$$

where the term in brackets on the RHS is the NTK, (2).⁸

Now suppose we’re allowed to truncate \dots while maintaining a controlled approximation to the function learned by the neural network. Moreover, let’s specialize to MSE loss. This yields

$$f_i(x, W_\mu(t+1)) - f_i(x, W_\mu(t)) = -\eta \sum_j \sum_{\alpha \in \mathcal{D}} (f_j(x_\alpha, t) - y_{j,\alpha}) K_{ij}(x, x_\alpha). \quad (12)$$

If we could sum the LHS of (12) over all time steps t , we would get the desired closed-form formula for the function learned by the neural network in the linearized approximation. What remains is to get rid of the t -dependence on the RHS of (12). To do this, we apply (12) itself to the special case that the argument x on the LHS is a point x_α in the training set, yielding roughly $f_j(x_\alpha, t) - y_{j,\alpha} = (1 - \eta K)^{t+1} (f_j(x_\alpha, t=0) - y_{j,\alpha})$ up to indices. This turns the sum over time steps into a geometric series in $(1 - \eta K)$ whose resummation yields Eq. (1).

The mathematical assumption required for these steps to go through is that we must be able to discard the higher-order terms in eqs. (10) and (11). Roughly, this can be imposed at the level of the model architecture in a scaling limit where we make the model much wider than it is deep, while initializing the weights with a $1/\sqrt{\text{width}}$ scaling. See [Roberts et al. \[2022\]](#) for a pedagogical review, as well as theoretical motivation for the eNTK conjecture upon keeping terms in the Taylor expansion to next-to-leading order.

B Kernels used in this paper

For TMS, the model $f(x) = \text{ReLU}(W^T W x + b)$ (4) implies that

⁸Throughout this section we also use that the NTK itself is time independent in the lazy limit.

$$\frac{\partial f_i(x)}{\partial W_{ai'}} = g_i(x)(W_{ai}x_{i'} + \delta_{ii'}W_{ak}x_k) \quad (13)$$

for $g = 1$ if $(W^T W x + b) > 0$ else 0, and the kernel is

$$K_{ij}(x_1, x_2) = g_i(x_1)g_j(x_2)[(W^T W)_{ij}(x_1 \cdot x_2) + (x_1)_j(W^T W x_2)_i + (x_2)_i(W^T W x_1)_j + \delta_{ij}(W x_1 \cdot W x_2)]. \quad (14)$$

For the modular arithmetic experiment, $f(x) = W^{(2)}(W^{(1)}x)^2$ (6) implies the layer-1 Jacobian

$$\frac{\partial f_i(x)}{\partial W_{km}^{(1)}} = 2W_{ki}^{(2)}(W^{(1)}x)_k x_m \quad (15)$$

and hence, the layer-1 kernel

$$K_{ij}^{(1)}(x_1, x_2) = 4 \sum_k W_{ki}^{(2)} W_{kj}^{(2)} (W^{(1)}x_1)_k (W^{(1)}x_2)_k (x_1 \cdot x_2). \quad (16)$$

The layer-2 Jacobian is

$$\frac{\partial f_i(x)}{\partial W_{ki'}^{(2)}} = \delta_{ii'}(W^{(1)}x)_k^2, \quad (17)$$

hence the layer-2 kernel is

$$K_{ij}^{(2)}(x_1, x_2) = \delta_{ij} \sum_k (W^{(1)}x_1)_k^2 (W^{(1)}x_2)_k^2. \quad (18)$$

The total kernel is their sum, $K = K^{(1)} + K^{(2)}$. It could be interesting, and probably is tractable, to understand what properties of the weights and data lead to the mechanistic structure found in the main text. However, I'll leave this for future work.

C Graph smoothness algorithm

To rotate the eigenvectors in the Layer 1 cliff and obtain the plot on the RHS of Fig. 4 in section 4, we apply the following two-stage “per-axis graph smoothness” algorithm:

1. On the underlying two-torus of possible inputs (a, b) for the modular arithmetic problem, we first construct a (size (p^2, p^2)) unnormalized Laplacian matrix for each cycle to be the matrix s.t.

$$v^T L_a v = \sum_{a,b} (v_{a,b} - v_{a+1 \bmod p, b})^2, \quad (19)$$

$$v^T L_b v = \sum_{a,b} (v_{a,b} - v_{a, b+1 \bmod p})^2, \quad (20)$$

penalizing cases where entries in the (length p^2) vector v corresponding to lattice points that differ by 1 in the a, b directions respectively are not the same. In practice, the matrices L_a, L_b that realize (19), (20) are $L_1 \otimes I_p$ and $I_p \otimes L_1$ respectively, for L_1 the dimension (p, p) matrix with 2 on the diagonal and -1 along diagonals offset by 1 and at the wrap-around entries $(1, p)$ and $(p, 1)$.

2. We diagonalize one of the two Laplacians, WLOG L_a , inside the span of the Layer 1 cliff. Concretely, we first compress L_a by computing $A = c^T L_a c$ for $c \in \mathbb{R}^{N,k}$ the column-orthonormalized collection of eNTK eigenvectors in the Layer 1 cliff, then eigendecompose

the compressed Laplacian finding $A = U\Sigma U^T$ with $U \in \mathbb{R}^{k,k}$, and finally rotate the eNTK cliff by the eigenvector matrix of the compressed Laplacian, $c' = cU$. This sorts the directions in the cliff by a -smoothness.⁹

3. We then take the directions in the cliff corresponding to the bottom half of the L_a eigenvalues¹⁰ and diagonalize L_b inside that span using the same procedure as step 2, sorting those directions by b -smoothness.

The logic is that if the Layer 1 eNTK cliff was spanned exactly by $(\cos a, \sin a)$, $(\cos b, \sin b)$ Fourier families, then we would expect the spectrum wrt L_a to contain degenerate near-zero values corresponding to the ‘ b ’ Fourier modes that are constant in the ‘ a ’ direction, followed by a tower of increasing pairs of nonzero eigenvalues corresponding to the sorted ‘ a ’ Fourier modes. So the two-stage process would sequentially disentangle them, and indeed this is what we find.

D Evolution of the sum/difference Fourier modes throughout training in the modular arithmetic experiment

In this section, we show that in the modular arithmetic experiment,

1. The second eigenvalue cliff in the full eNTK spectrum (left-hand column of Fig. 2) approximately contains the ‘sum’ and ‘difference’ Fourier feature families $(\cos a \pm b, \sin a \pm b)$.
2. The features themselves form continuously to either side of the grokking phase transition.

To see this, we apply the graph smoothness algorithm in Appendix C to the sum and difference families, first constructing Laplacians

$$v^T L_{\text{sum}} v = \sum_{a,b} (v_{a,b} - v_{a+1 \bmod p, b+1 \bmod p})^2, \quad (21)$$

$$v^T L_{\text{diff}} v = \sum_{a,b} (v_{a,b} - v_{a+1 \bmod p, b-1 \bmod p})^2, \quad (22)$$

that penalize variation along the diagonals, then diagonalizing first the sum then the difference Laplacian within the span of the second eigenvalue cliff. This situation is equivalent to two-stage diagonalization in the a and b directions up to a 45-degree rotation, so the logic of Appendix C goes through. In particular, (a, b) and $(a+1, b+1)$ have the same $a-b$, so the difference family is flat wrt L_{sum} , and vice versa.

The results are shown in Fig. 5. From the bottom right plot showing the results of disentanglement at the end of training, we see that the second eigenvalue cliff approximately contains the sum and difference families. (The heatmaps for each family form a “ $>$ ” shape because stepping across the diagonal advances the argument of each Fourier mode by $2 \cdot 2\pi k/p$, so the Laplacian energy is minimal near $k \approx 0$ and $k \approx p/2$, and maximal near $k \approx p/4$.) The disentanglement is imperfect because the low-energy “ $k = 1$ ” and “ $k = 14$ ” sum modes mix with the L_{diff} modes¹¹, but the association of the second cliff with sum/diff Fourier families is clearly approximately correct.

⁹In a sentence, this is because directions where we minimize $v^T L_a v$ in a given vector space are the smoothest directions in the vector space by the operational definition (19) of the Laplacian, and we can minimize this from an eigendecomposition by the Rayleigh-Ritz theorem.

¹⁰I.e. the bottom $2 \lfloor \frac{p}{2} \rfloor$ directions in practice.

¹¹Indeed, we can make the heatmaps in Fig 5 appear closer to 1:1 by diagonalizing L_{diff} in Step 3 of the algorithm described in Appendix C over the bottom half + 4 instead of bottom half of L_{sum} eigenvalues to unmix them (although I haven’t included the plots that result from doing this here).

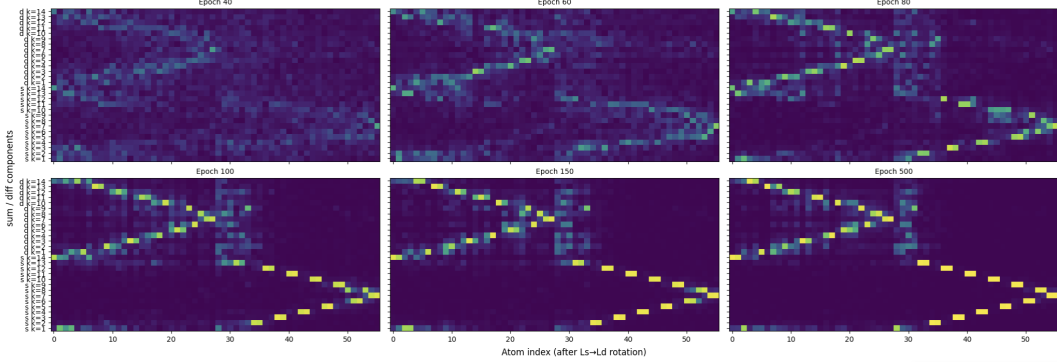


Figure 5: Results from applying the two-stage graph smoothness algorithm described in Appendix C wrt the sum and difference Laplacians (21), (22) to rotate the eNTK eigenvectors in the second eigenvalue cliff of the modular arithmetic experiment at different epochs. Each plot is a heatmap showing the squared norm of the inner product of rotated basis vectors in the second eigenvalue cliff with the $(\cos a + b, \sin a + b)$ or $(\cos a - b, \sin a - b)$ feature families.

Moreover, from comparing the change in heatmaps between epochs 80-100 (when grokking happens) and the other epochs, we see that nothing special happens at the grokking phase transition at the level of the eNTK eigenvectors. Instead, incipient alignment of the second cliff eigenvectors with the sum/diff modes was visible well before the phase transition, and continues after it. As discussed in the main text, the eigenvalues associated with the second cliff do jump in magnitude at the grokking phase transition.

References

Guillaume Alain and Yoshua Bengio. Understanding intermediate layers using linear classifier probes. [arXiv preprint arXiv:1610.01644](https://arxiv.org/abs/1610.01644), 2016.

Alexander Atanasov, Blake Bordelon, and Cengiz Pehlevan. Neural networks as kernel learners: The silent alignment effect. [ICLR 2022](https://arxiv.org/pdf/2111.00034.pdf), 11 2021. URL <https://arxiv.org/pdf/2111.00034.pdf>.

Aristide Baratin, Thomas George, César Laurent, R Devon Hjelm, Guillaume Lajoie, Pascal Vincent, and Simon Lacoste-Julien. Implicit regularization via neural feature alignment. In [International Conference on Artificial Intelligence and Statistics](https://proceedings.mlr.press/v132/lajoie21a.html), pages 2269–2277. PMLR, 2021.

Trenton Bricken, Adly Templeton, Joshua Batson, Brian Chen, Adam Jermyn, Tom Conerly, Nick Turner, Cem Anil, Carson Denison, Amanda Askell, et al. Towards monosemanticity: Decomposing language models with dictionary learning. [Transformer Circuits Thread](https://transformer-circuits.com/towards-monosemanticity-decomposing-language-models-with-dictionary-learning), 2, 2023.

Lucius Bushnaq, Jake Mendel, Stefan Heimersheim, Dan Braun, Nicholas Goldowsky-Dill, Kaarel Hänni, Cindy Wu, and Marius Hobbhahn. Using degeneracy in the loss landscape for mechanistic interpretability. In [ICML 2024 Workshop on Mechanistic Interpretability](https://icml.cc/2024/Workshop/MechanisticInterpretability), 2024.

Nelson Elhage, Tristan Hume, Catherine Olsson, Nicholas Schiefer, Tom Henighan, Shauna Kravec, Zac Hatfield-Dodds, Robert Lasenby, Dawn Drain, Carol Chen, Roger Grosse, Sam McCandlish, Jared Kaplan, Dario Amodei, Martin Wattenberg, and Christopher Olah. Toy models of superposition. [Transformer Circuits Thread](https://transformer-circuits.com/toy-models-of-superposition), 2022.

Stanislav Fort, Gintare Karolina Dziugaite, Mansheej Paul, Sepideh Kharaghani, Daniel M Roy, and Surya Ganguli. Deep learning versus kernel learning: an empirical study of loss landscape geometry and the time evolution of the neural tangent kernel. [Advances in Neural Information Processing Systems](https://proceedings.neurips.cc/paper/2020/file/5850-5861.pdf), 33:5850–5861, 2020.

Lauren Greenspan. Renormalizing interpretability. URL: <https://www.lesswrong.com/s/3fkngqkujhgrnrodA>, 2025.

Andrey Gromov. Grokking modular arithmetic. [arXiv preprint arXiv:2301.02679](https://arxiv.org/abs/2301.02679), 2023.

Roger Grosse, Juhan Bae, Cem Anil, Nelson Elhage, Alex Tamkin, Amirhossein Tajdini, Benoit Steiner, Dustin Li, Esin Durmus, Ethan Perez, et al. Studying large language model generalization with influence functions. [arXiv preprint arXiv:2308.03296](https://arxiv.org/abs/2308.03296), 2023.

Tom Henighan, Shan Carter, Tristan Hume, Nelson Elhage, Robert Lasenby, Stanislav Fort, Nicholas Schiefer, and Christopher Olah. Superposition, memorization, and double descent. [Transformer Circuits Thread](https://transformer-circuits.com/superposition-memorization-and-double-descent), 6:24, 2023.

Arthur Jacot, Franck Gabriel, and Clément Hongler. Neural tangent kernel: Convergence and generalization in neural networks. [Advances in neural information processing systems](https://proceedings.neurips.cc/paper/2018/file/3f2e4b46d2d37004c2f3c62b4b8235d9.pdf), 31, 2018.

Pang Wei Koh and Percy Liang. Understanding black-box predictions via influence functions. In [International conference on machine learning](https://proceedings.mlr.press/v70/koh17a.html), pages 1885–1894. PMLR, 2017.

Kenneth Li, Aspen K Hopkins, David Bau, Fernanda Viégas, Hanspeter Pfister, and Martin Wattenberg. Emergent world representations: Exploring a sequence model trained on a synthetic task. [ICLR](https://arxiv.org/abs/2303.13700), 2023.

Noel Loo, Ramin Hasani, Alexander Amini, and Daniela Rus. Evolution of neural tangent kernels under benign and adversarial training. *Advances in Neural Information Processing Systems*, 35: 11642–11657, 2022.

Mohamad Amin Mohamadi, Wonho Bae, and Danica J Sutherland. A fast, well-founded approximation to the empirical neural tangent kernel. In *International conference on machine learning*, pages 25061–25081. PMLR, 2023.

Neel Nanda. Attribution patching: Activation patching at industrial scale. [URL: https://www.neelnanda.io/mechanistic-interpretability/attribution-patching](https://www.neelnanda.io/mechanistic-interpretability/attribution-patching), 2023.

Neel Nanda, Lawrence Chan, Tom Lieberum, Jess Smith, and Jacob Steinhardt. Progress measures for grokking via mechanistic interpretability. *arXiv preprint arXiv:2301.05217*, 2023.

Chris Olah. Mechanistic interpretability, variables, and the importance of interpretable bases. [URL:https://www.transformer-circuits.pub/2022/mech-interp-essay](https://www.transformer-circuits.pub/2022/mech-interp-essay), 2022.

Chris Olah, Nick Cammarata, Ludwig Schubert, Gabriel Goh, Michael Petrov, and Shan Carter. Zoom in: An introduction to circuits. *Distill*, 2020. doi: 10.23915/distill.00024.001. <https://distill.pub/2020/circuits/zoom-in>.

Catherine Olsson, Nelson Elhage, Neel Nanda, Nicholas Joseph, Nova DasSarma, Tom Henighan, Ben Mann, Amanda Askell, Yuntao Bai, Anna Chen, Tom Conerly, Dawn Drain, Deep Ganguli, Zac Hatfield-Dodds, Danny Hernandez, Scott Johnston, Andy Jones, Jackson Kernion, Liane Lovitt, Kamal Ndousse, Dario Amodei, Tom Brown, Jack Clark, Jared Kaplan, Sam McCandlish, and Chris Olah. In-context learning and induction heads. *Transformer Circuits Thread*, 2022. <https://transformer-circuits.pub/2022/in-context-learning-and-induction-heads/index.html>.

Guillermo Ortiz-Jiménez, Seyed-Mohsen Moosavi-Dezfooli, and Pascal Frossard. What can linearized neural networks actually say about generalization? *Advances in Neural Information Processing Systems*, 34:8998–9010, 2021.

Alethea Power, Yuri Burda, Harri Edwards, Igor Babuschkin, and Vedant Misra. Grokking: Generalization beyond overfitting on small algorithmic datasets. *arXiv preprint arXiv:2201.02177*, 2022.

Daniel A Roberts, Sho Yaida, and Boris Hanin. *The principles of deep learning theory*, volume 46. Cambridge University Press Cambridge, MA, USA, 2022.

Lee Sharkey, Bilal Chughtai, Joshua Batson, Jack Lindsey, Jeff Wu, Lucius Bushnaq, Nicholas Goldowsky-Dill, Stefan Heimersheim, Alejandro Ortega, Joseph Bloom, et al. Open problems in mechanistic interpretability. *arXiv preprint arXiv:2501.16496*, 2025.

Nikolaos Tsilivis and Julia Kempe. What can the neural tangent kernel tell us about adversarial robustness? *Advances in Neural Information Processing Systems*, 35:18116–18130, 2022.